Monthly Notices
of the
ROYAL ASTRONOMICAL SOCIETY

MNRAS **464,** 3005–3012 (2017)
Advance Access publication 2016 October 8

doi:10.1093/mnras/stw2602

Modelling galaxy clustering on small scales to tighten constraints on dark energy and modified gravity

Yun Wang[1,2]★

[1]*IPAC, California Institute of Technology, Mail Code 314-6, 1200 East California Boulevard, Pasadena, CA 91125, USA*
[2]*Homer L. Dodge Department of Physics and Astronomy, University of Oklahoma, 440 W Brooks Street, Norman, OK 73019, USA*

Accepted 2016 October 7. Received 2016 October 3; in original form 2016 June 30; Editorial Decision 2016 October 6

ABSTRACT

We present a new approach to measuring cosmic expansion history and growth rate of large-scale structure using the anisotropic two-dimensional galaxy correlation function (2DCF) measured from data; it makes use of the empirical modelling of small-scale galaxy clustering derived from numerical simulations by Zheng et al. We validate this method using mock catalogues, before applying it to the analysis of the CMASS sample from the Sloan Digital Sky Survey Data Release 10 of the Baryon Oscillation Spectroscopic Survey. We find that this method enables accurate and precise measurements of cosmic expansion history and growth rate of large-scale structure. Modelling the 2DCF fully including non-linear effects and redshift space distortions in the scale range of 16–144 h^{-1} Mpc, we find $H(0.57)r_{\rm s}(z_{\rm d})/c = 0.0459 \pm 0.0006$, $D_{\rm A}(0.57)/r_{\rm s}(z_{\rm d}) = 9.011 \pm 0.073$, and $f_{\rm g}(0.57)\sigma_8(0.57) = 0.476 \pm 0.050$, which correspond to precisions of 1.3 per cent, 0.8 per cent, and 10.5 per cent, respectively. We have defined $r_{\rm s}(z_{\rm d})$ to be the sound horizon at the drag epoch computed using a simple integral, $f_{\rm g}(z)$ as the growth rate at redshift z, and $\sigma_8(z)$ as the matter power spectrum normalization on $8\,h^{-1}$ Mpc scale at z. We find that neglecting the small-scale information significantly weakens the constraints on $H(z)$ and $D_{\rm A}(z)$, and leads to a biased estimate of $f_{\rm g}(z)$. Our results indicate that we can significantly tighten constraints on dark energy and modified gravity by reliably modelling small-scale galaxy clustering.

Key words: cosmology: observations – distance scale – large-scale structure of universe.

1 INTRODUCTION

Almost two decades after the first detections of cosmic acceleration (Riess et al. 1998; Perlmutter et al. 1999), we are still in the dark about its nature. We do not even know if this cosmic acceleration is caused by dark energy (an unknown energy component in the Universe) or modified gravity (a modification of general relativity).[1]

The distribution of galaxies in the Universe traces cosmic large-scale structure, and is a powerful probe of the nature of cosmic acceleration. Galaxy clustering enables the measurement of cosmic expansion history in two complementary ways (Blake & Glazebrook 2003; Seo & Eisenstein 2003): through the direct measurement of $H(z)$, the Hubble parameter (the cosmic expansion rate $\mathrm{d}\ln a(t)/\mathrm{d}t$, where $a(t)$ is the cosmic scale factor), and $D_{\rm A}(z)$, the angular-diameter distance, which constrains $H(z)$ in an integral form. The measurement of $H(z)$ allows us to determine the time dependence of dark energy. The fact that we measure the redshifts of galaxies (and not their distances directly) leads to artefacts in the observed galaxy distribution, the redshift space distortions (RSD). On large scales, the RSD are linear and enable the measurement of the linear growth rate of cosmic large-scale structure $f_{\rm g}(z)$ (Kaiser 1987), which enables us to differentiate between dark energy and modified gravity as the cause for cosmic acceleration, given the expansion history measurement (Guzzo et al. 2008; Wang 2008).

The largest set of galaxy-clustering data comes from the Baryon Oscillation Spectroscopic Survey (BOSS) [part of the Sloan Digital Sky Survey (SDSS) III][2], which should yield millions of galaxy redshifts up to $z = 0.7$ over 10 000 deg^2. BOSS has completed its observations in 2014. The portfolio of ongoing and planned future galaxy redshift surveys is diverse and exciting. The eBOSS survey[3] (2014–2020) plans to cover over 7500 deg^2 for luminous red galaxies (LRGs) in the redshift range of $0.6 < z < 0.8$, and over 1500 deg^2 for [O II] emission line galaxies (ELGs) in the redshift range of $0.6 < z < 1$. The Dark Energy Spectroscopic Instrument

★ E-mail: wang@ipac.caltech.edu

[1] For reviews, see e.g. Ratra & Vogeley (2008), Frieman, Turner & Huterer (2008), Caldwell & Kamionkowski (2009), Uzan (2010), Wang (2010), Li et al. (2011), and Weinberg et al. (2013).

[2] http://www.sdss3.org/surveys/boss.php
[3] http://www.sdss.org/surveys/eboss/

survey[4] (2018–2022) will cover over 14 000 deg^2 for LRGs ($0.1 < z < 1.1$) and [O II] ELGs ($0.1 < z \lesssim 1.7$). *Euclid*,[5] an ESA-led space mission scheduled for launch in 2020, will obtain galaxy redshifts for Hα ELGs over 15 000 deg^2 over a wide redshift range up to $z = 2$ (Laureijs et al. 2011). *Wide-Field Infrared Survey Telescope* (*WFIRST*)[6] is NASA's next flagship mission in astrophysics, with a launch date in 2025. *WFIRST* is capable of a great range of possible galaxy redshift surveys of Hα and [O III] ELGs, in the redshift range of 1–3; it will likely carry out a very deep galaxy redshift survey over at least 2000 deg^2 that is complementary to the very wide galaxy redshift survey by *Euclid* (Spergel et al. 2015).

In order to fully realize the scientific potential of the ongoing and planned future surveys, it is important that we use BOSS data to develop and test optimal approaches to extracting information on dark energy and modified gravity from galaxy-clustering data. Since the BOSS final data release (DR12) has not yet taken place, we use BOSS Data Release 10 (DR10) in this paper to explore the accurate modelling of small-scale galaxy-clustering data in the context of the anisotropic analysis of the two-dimensional galaxy correlation function (2DCF). We use a Markov Chain Monte Carlo (MCMC)-based model-independent approach to measure $H(z)$, $D_{\rm A}(z)$, and $f_{\rm g}(z)\sigma_8(z)$ (Song & Percival 2009, with $\sigma_8(z)$ denoting the matter power spectrum normalization on $8\,h^{-1}$ Mpc scale at z), and marginalize over matter density $\Omega_{\rm m}\,h^2$, baryon density $\Omega_{\rm b}\,h^2$, power-law index of the primordial matter power spectrum $n_{\rm s}$, normalization of the matter power spectrum today P_0, as well as parameters used to model non-linear effects and RSD. This conservative approach enables the combination of our results with other data to probe dark energy and gravity.

Our methodology is presented in Section 2. Our results are shown in Section 3. We summarize and conclude in Section 4.

2 METHODOLOGY

2.1 Modelling the galaxy correlation function

Our methodology is based on Wang (2014), with the RSD modelling modified as per Zheng et al. (2013, based on the work of Zhang, Pan & Zheng 2013):

$$P(\boldsymbol{k})^{\rm g,s}_{\rm dw,nl} = b^2 P(\boldsymbol{k})_{\rm dw,nl}\left[1+\beta\tilde{W}(k,z)\mu^2\right]^2, \quad (1)$$

where $P(\boldsymbol{k})^{\rm g,s}_{\rm dw,nl}$ is the redshift space galaxy power spectrum, $P(\boldsymbol{k})_{\rm dw,nl}$ is the matter power spectrum, b is the bias between galaxy and matter distributions, β is the linear RSD parameter, and μ is the cosine of the angle between $\boldsymbol{k}$ and the line of sight. The window function $\tilde{W}(k,z)$ takes the form (Zheng et al. 2013)

$$\tilde{W}(k,z) = \frac{1}{1+\Delta\alpha(z)\Delta^2(k,z)}. \quad (2)$$

We find that it is simplest to choose $\Delta^2(k,z) = k^3 P_{\rm lin}/(2\pi^2)$, with the linear power spectrum given by

$$P_{\rm lin} = P_0 k^{n_{\rm s}} T^2(k), \quad (3)$$

where $T(k)$ is the linear matter transfer function.

The non-linear dewiggled matter power spectrum is

$$P_{\rm dw,nl} = F_{\rm NL}(k)\,P_{\rm dw,lin}(\boldsymbol{k}), \quad (4)$$

with $F_{\rm NL}(k)$ modelling non-linear evolution and scale-dependent bias (Cole et al. 2005):

$$F_{\rm NL}(k) = \frac{1+Qk^2}{1+f_{\rm A}k+Bk^2}. \quad (5)$$

We take $B = Q/10$ (Sanchez, Baugh & Angulo 2008). We can write the linear dewiggled power spectrum as

$$P_{\rm dw,lin}(\boldsymbol{k}) = G^2(z)P_0k^{n_{\rm s}}\left\{T^2_{\rm nw}(k)+T^2_{\rm BAO}(k)e^{-g_\mu k^2/(2k_*^2)}\right\}, \quad (6)$$

where we have defined

$$T^2_{\rm BAO}(k) = T^2(k) - T^2_{\rm nw}(k), \quad (7)$$

with $T_{\rm nw}(k)$ denoting the pure cold dark matter (CDM; no baryons) transfer function given by equation (29) from Eisenstein & Hu (1998). The non-linear damping factor, $\mathrm{e}^{-g_\mu k^2/(2k_*^2)}$, was derived using N-body simulations by Eisenstein, Seo & White (2007); g_μ describes the enhanced damping along the line of sight due to the enhanced power:

$$g_\mu(\boldsymbol{k},z) \equiv G^2(z)\{1-\mu^2+\mu^2[1+f_{\rm g}(z)]^2\}. \quad (8)$$

Since density perturbations grow with cosmic time, the linear regime expands as we go to higher redshifts. This is why the scale of the linear regime increases with $1/G(z)$ at high redshifts, while g_μ scales with the linear growth factor $G(z)$ squared.

The 2DCF, our model to be compared with data, is obtained by convolving $\tilde{\xi}$, the Fourier transform of the redshift space galaxy power spectrum $P(\boldsymbol{k})^{\rm g,s}_{\rm dw,nl}$, with the probability distribution of galaxy peculiar velocities $f(v)$:

$$\xi(\sigma,\pi) = \int_{-\infty}^{\infty}\tilde{\xi}\left(\sigma,\pi-\frac{v}{H(z)a(z)}\right)f(v)\mathrm{d}v, \quad (9)$$

where $H(z)$ is the Hubble parameter and $a(z)$ is the cosmic scale factor, and $f(v)$ is given by

$$f(v) = \frac{1}{\sigma_{\rm v}\sqrt{2\pi}}\exp\left(-\frac{v^2}{2\sigma_{\rm v}^2}\right), \quad (10)$$

with $\sigma_{\rm v}$ denoting the galaxy peculiar velocity dispersion. Zheng et al. (2013) showed that this Gaussian $f(v)$ matches better with their RSD modelling, compared to the usual form of $f(v) = (\sigma_{\rm v}\sqrt{2})^{-1}\exp(-\sqrt{2}|v|/\sigma_{\rm v})$.

To save computational time in obtaining the Fourier transform of $P(\boldsymbol{k})^{\rm g,s}_{\rm dw,nl}$, we write

$$\begin{aligned} P(\boldsymbol{k})^{\rm g,s}_{\rm dw,nl} &= P(\boldsymbol{k})^{\rm g,s}_{\rm nw,nl} + (\boldsymbol{k})^{\rm g,s}_{\rm BAO,dw,nl},\\ P(\boldsymbol{k})^{\rm g,s}_{\rm nw,nl} &= b^2G^2(z)\left[1+\beta\tilde{W}(k)\mu^2\right]^2 P_0k^{n_{\rm s}}T^2_{\rm nw}(k)F_{\rm NL}(k),\\ P(\boldsymbol{k})^{\rm g,s}_{\rm BAO,dw,nl} &= b^2G^2(z)\left[1+\beta\tilde{W}(k)\mu^2\right]^2 P_0k^{n_{\rm s}}T^2_{\rm BAO}(k)\\ &\quad\times F_{\rm NL}(k)\mathrm{e}^{-g_\mu k^2/(2k_*^2)}. \end{aligned} \quad (11)$$

This leads to two terms in the Fourier transform of $P(\boldsymbol{k})^{\rm g,s}_{\rm dw,nl}$ with different dependence on μ:

$$\tilde{\xi}(\sigma,\pi) = \xi^{\rm g,s}_{\rm nw}(\sigma,\pi) + \xi^{\rm g,s}_{\rm BAO,dw}(\sigma,\pi), \quad (12)$$

with σ and π denoting the transverse and line-of-sight separations of a pair of galaxies, respectively. The second term is the Fourier transform of $P(\boldsymbol{k})^{\rm g,s}_{\rm BAO,dw,nl}$, which is more complicated due to the additional damping factor $\mathrm{e}^{-g_\mu k^2/(2k_*^2)}$, with g_μ dependent on μ (see equation 8). Chuang & Wang (2013) found an easy way to deal with this by noting that the μ-dependent damping factor in k-space

[4] http://desi.lbl.gov/
[5] http://www.euclid-ec.org/
[6] http://wfirst.gsfc.nasa.gov/

becomes a Gaussian convolution in configuration space (Chuang & Wang 2013):

$$\xi^{\rm g,s}_{\rm BAO,dw}(\sigma,\pi) = \frac{1}{\sigma_\star\sqrt{\pi}}\int_{-\infty}^{\infty} {\rm d}x\, \xi^{\rm g,s}_{\rm BAO,sdw}(\sigma,\pi-x)\,{\rm e}^{-x^2/\sigma_\star^2}, \quad (13)$$

where $\xi^{\rm g,s}_{\rm BAO,sdw}(\sigma,\pi)$ is the Fourier transform of $P(\boldsymbol{k})^{\rm g,s}_{\rm BAO,dw,nl}$ with the damping factor ${\rm e}^{-g_\mu k^2/(2k_\star^2)}$ replaced by its μ-independent part, ${\rm e}^{-G^2(z)k^2/(2k_\star^2)}$, and

$$\sigma_\star^2 = \frac{[4f_{\rm g}(z)+2f_{\rm g}^2(z)]G^2(z)}{k_\star^2}. \quad (14)$$

To calculate $\xi^{\rm g,s}_{\rm nw}(\sigma,\pi)$ and $\xi^{\rm g,s}_{\rm BAO,sdw}(\sigma,\pi)$, we take the Fourier transform of

$$P_x(\boldsymbol{k})^{\rm s} = P_x(k)\left[1+\beta\tilde{W}(k,z)\mu^2\right]^2. \quad (15)$$

This gives us

$$\begin{aligned}\tilde{\xi}^x(\sigma,\pi) = {}& \xi^x(r)+2\beta\mu^2\tilde{\xi}^x(r)+\beta^2\mu^4\tilde{\xi}^x_2(r)\\ &+\frac{2}{3}\beta\left(1-3\mu^2\right)\tilde{\bar{\xi}}^x(r)\\ &+\frac{\beta^2}{2}\left\{\left(1-6\mu^2+5\mu^4\right)\tilde{\bar{\xi}}^x_2(r)\right.\\ &\left.-\frac{1}{5}\left(3-30\mu^2+35\mu^4\right)\tilde{\bar{\bar{\xi}}}^x_2(r)\right\},\end{aligned} \quad (16)$$

where the superscript x represents 'nw' or 'BAO,sdw'. The function $\xi^x(r)$ is the Fourier transform of $P_x(k)$; $\tilde{\xi}^x(r)$, $\tilde{\xi}^x_2(r)$, $\tilde{\bar{\xi}}^x(r)$, and $\tilde{\bar{\bar{\xi}}}^x_2(r)$ are related integrals that depend on the window function $\tilde{W}(k)$. These are defined as follows:

$$\xi^x(r) = \frac{1}{2\pi^2}\int_0^\infty {\rm d}k\,k^2P_x(k)\left[\frac{\sin(kr)}{kr}\right] \quad (17)$$

$$\tilde{\xi}^x(r) = \frac{1}{2\pi^2}\int_0^\infty {\rm d}k\,k^2\tilde{W}(k)P_x(k)\left[\frac{\sin(kr)}{kr}\right] \quad (18)$$

$$\tilde{\xi}^x_2(r) = \frac{1}{2\pi^2}\int_0^\infty {\rm d}k\,k^2\tilde{W}^2(k)P_x(k)\left[\frac{\sin(kr)}{kr}\right] \quad (19)$$

$$\tilde{\bar{\xi}}^x(r) = \frac{3}{r^3}\int_0^r {\rm d}s\,s^2\tilde{\xi}^x(s) \quad (20)$$

$$\tilde{\bar{\xi}}^x_2(r) = \frac{3}{r^3}\int_0^r {\rm d}s\,s^2\tilde{\xi}^x_2(s) \quad (21)$$

$$\tilde{\bar{\bar{\xi}}}^x_2(r) = \frac{5}{r^5}\int_0^r {\rm d}s\,s^4\tilde{\xi}^x_2(s). \quad (22)$$

Equations (16)–(22) give us $\xi^{\rm g,s}_{\rm nw}(\sigma,\pi)$ and $\xi^{\rm g,s}_{\rm BAO,sdw}(\sigma,\pi)$, with $P_x(k)$ given by

$$P_{\rm nw}(k) = b^2G^2(z)P_0k^{n_{\rm s}}T^2_{\rm nw}(k)F_{\rm NL}(k) \quad (23)$$

$$\begin{aligned}P_{\rm BAO,sdw}(k) = {}& b^2G^2(z)P_0k^{n_{\rm s}}T^2_{\rm BAO}(k)F_{\rm NL}(k)\\ &\times{\rm e}^{-G^2(z)k^2/(2k_\star^2)},\end{aligned} \quad (24)$$

respectively. It is straightforward to check that equations (16)–(22) give the standard expression for $\xi^{\rm s}(\sigma,\pi)$ in terms of $P(\boldsymbol{k})$ (Hamilton 1992), if we set $\tilde{W}=1$.

2.2 Data and covariance matrix

We use the publicly available CMASS sample from BOSS DR10 (Anderson et al. 2014). The DR10 CMASS sample consists of 540 147 galaxies over an effective area of 6161 deg^2, with 420 696 galaxies over an effective area of 4817 deg^2 in the Northern Galactic Cap, and 119 451 galaxies over 1345 deg^2 in the Southern Galactic Cap. The CMASS sample is designed to be approximately stellar-mass- limited for $z>0.45$. The galaxies are colour selected, with a median redshift of 0.57.

The CMASS sample from DR10 has roughly twice the galaxy number and effective area compared to the CMASS sample from DR9, which consists of 264 283 galaxies over an effective area of 3275 deg^2. We used DR9 in Wang (2014); it is appropriate for us to use DR10 in this paper to demonstrate our improved modelling to extract small-scale cosmological information.

Mock catalogues are required to compute the covariance matrix for the data sample, and to validate our analysis technique. We use the set of 600 mocks for BOSS DR10. For a detailed description of these mocks,[7] see Manera et al. (2013, 2015). The input cosmological model of the mock catalogues is ΛCDM model with $\Omega_k=0$, $h=0.7$, $\Omega_{\rm m}h^2=0.13426$ ($\Omega_{\rm m}=0.274$), $\Omega_{\rm b}h^2=0.0224$ ($\Omega_{\rm b}=0.0457$), $n_{\rm s}=0.95$, and $\sigma_8=0.8$. We use this model as the fiducial model for our data analysis.

Before carrying out our analysis of galaxy clustering, we need to convert measured redshifts of galaxies to comoving distances. We use the fiducial model to make this conversion. Since our measurements of $H(z)$, $D_{\rm A}(z)$, and $f_{\rm g}(z)$ are made through scaling (see Section 2.3), our results are not sensitive to the assumed fiducial model.

To measure the 2DCF from data, we use the estimator (Landy & Szalay 1993)

$$\xi(\sigma,\pi) = \frac{{\rm DD}(\sigma,\pi)-2{\rm DR}(\sigma,\pi)+{\rm RR}(\sigma,\pi)}{{\rm RR}(\sigma,\pi)}, \quad (25)$$

where σ and π are the transverse and line-of-sight separations of a pair of galaxies in the sky. DD, DR, and RR represent the normalized data–data, data–random, and random–random pair counts, respectively, in a given distance range. The line of sight is defined as the direction from the observer to the centre of a pair. We use a bin size of 8 h^{-1} Mpc $\times$ 8 h^{-1} Mpc. The estimator in equation (25) has minimal variance for a Poisson process. We use the random data sets that accompany the BOSS data sets, which have the same radial and angular selection functions as the real data. To mitigate various systematic effects, the BOSS catalogues include weights that should be applied to each galaxy.

We calculate the 2DCF of the 600 mock catalogues, and use these to construct the covariance matrix of the measured 2DCF as follows:

$$C_{ij} = \frac{1}{N-1}\sum_{k=1}^{N}(\bar{\xi}_i-\xi_i^k)(\bar{\xi}_j-\xi_j^k), \quad (26)$$

where N is the number of the mock catalogues ($N=600$), $\bar{\xi}_m$ is the mean of the mth bin of the mock catalogue correlation functions, and ξ_m^k is the value in the mth bin of the kth mock catalogue correlation function. To correct the underestimate of the errors due to the finite number of mocks, we multiply the inverse covariance matrix by a factor of $(N-N_{\rm data}-1)/(N-1)$, where $N_{\rm data}$ is the number of data points used in our analysis (Hartlap, Simon & Schneider 2007).

2.3 The likelihood analysis

We follow the approach of Chuang & Wang (2012) and Wang (2014) in our likelihood analysis. If the measurements are Gaussian

[7] http://www.marcmanera.net/mocks/

distributed, the likelihood of a model given the data is proportional to $\exp(-\chi^2/2)$ (Press et al. 1992), where χ^2 compares data with model predictions. We run MCMC (Lewis & Bridle 2002), and assume the likelihood $\mathcal{L} \propto \exp(-\chi^2/2)$ in the acceptance function, with

$$\chi^2 \equiv \sum_{i,j=1}^{N_{\rm bins}} \left[\xi_{\rm th}(\boldsymbol{s}_i) - \xi_{\rm obs}(\boldsymbol{s}_i)\right] C_{ij}^{-1} \left[\xi_{\rm th}(\boldsymbol{s}_j) - \xi_{\rm obs}(\boldsymbol{s}_j)\right], \quad (27)$$

where $\xi_{\rm th}$ (see Section 2.1) and $\xi_{\rm obs}$ (see Section 2.2) are the model and observed correlation functions, respectively. $N_{\rm bins}$ is the number of data bins used, and $\boldsymbol{s}_i = (\sigma_i, \pi_i)$.

For efficient and consistent implementation in the numerical analysis, we avoid re-measuring the 2DCF from data for each model to obtain $\xi_{\rm obs}$ in that model. Instead, we use scaling to re-write equation (27), such that the model $\xi_{\rm th}$ is scaled in a consistent manner to be compared to the $\xi_{\rm obs}$ measured assuming the fiducial model. This works because the fiducial model is only used in converting redshifts into distances for the galaxies in our data sample; assuming different models in converting redshifts into distances results in observed galaxy distributions that are related by a simple scaling of the galaxy separations. To derive this scaling, note that the separations of galaxies in angle and redshift are observables, thus independent of the model assumed, i.e.

$$\Delta\theta = \frac{\sigma}{D_{\rm A}(z)} = \frac{\sigma_{\rm fid}}{D_{\rm A}^{\rm fid}(z)} \quad (28)$$

$$\Delta z = H(z)\pi = H^{\rm fid}(z)\pi_{\rm fid}, \quad (29)$$

where the label "fid' refers to parameters in the fiducial model, while the parameters without the label represent an arbitrary model. For a thin redshift shell, we can now convert the galaxy separations from the fiducial model to another model using the scaling (see e.g. Seo & Eisenstein 2003)

$$(\sigma, \pi) = \left(\frac{D_{\rm A}(z)}{D_{\rm A}^{\rm fid}(z)}\sigma_{\rm fid}, \frac{H^{\rm fid}(z)}{H(z)}\pi_{\rm fid}\right). \quad (30)$$

This means that the measured 2DCFs, assuming an arbitrary model and the fiducial model, are related as follows:

$$\xi_{\rm obs}(\sigma, \pi) = T\left(\xi_{\rm obs}^{\rm fid}(\sigma_{\rm fid}, \pi_{\rm fid})\right), \quad (31)$$

with T denoting the mapping given by equation (30).

Now the χ^2 from equation (27) can be rewritten as (Chuang & Wang 2012)

$$\chi^2 \equiv \sum_{i,j=1}^{N_{\rm bins}} \left\{T^{-1}\left[\xi_{\rm th}(\boldsymbol{s}_i)\right] - \xi_{\rm obs}^{\rm fid}(\boldsymbol{s}_i)\right\} C_{{\rm fid},ij}^{-1} \times \left\{T^{-1}\left[\xi_{\rm th}(\boldsymbol{s}_j)\right] - \xi_{\rm obs}^{\rm fid}(\boldsymbol{s}_j)\right\}, \quad (32)$$

with $C_{\rm fid}$ denoting the covariance matrix of the observed data assuming the fiducial model. The operator $T^{-1}\left[\xi_{\rm th}(\boldsymbol{s}_i)\right]$ maps the model computed at $\{\sigma, \pi\}$ to the fiducial model frame coordinates ($\sigma_{\rm fid}$, $\pi_{\rm fid}$) as given by equation (30).

We find that it is most efficient to convert the grid of ($\sigma_{\rm fid}$, $\pi_{\rm fid}$) spanned by the measured 2DCF to a grid of $\{\sigma, \pi\}$ for each model using equation (30), using the $H(z)$ and $D_{\rm A}(z)$ assumed for that model. Then, we compute the 2DCF for the model on the grid of $\{\sigma, \pi\}$, which depends on the other parameters in the model: cosmological parameters $\Omega_{\rm m}h^2$, $\Omega_{\rm b}h^2$, $n_{\rm s}$, P_0, as well as non-linearity and RSD parameters β, k_*, $\Delta\alpha$, $f_{\rm g}$, $\sigma_{\rm v}$, Q, and $f_{\rm A}$. Finally, the model should be multiplied by a volume factor given by

$$V_{\rm fac} = \frac{H(z)}{H^{\rm fid}(z)}\left(\frac{D_{\rm A}^{\rm fid}(z)}{D_{\rm A}(z)}\right)^2. \quad (33)$$

Effectively, we are using the shape of the galaxy 2PCF as a standard ruler to measure $H(z)$ and $D_{\rm A}(z)$, with cosmological parameters ($\Omega_{\rm m}h^2$, $\Omega_{\rm b}h^2$, $n_{\rm s}$, P_0) and parameters that describe systematic effects (non-linearity and RSD) included as calibration parameters. With reliable modelling of RSD, our technique also allows the measurement of $f_{\rm g}(z)\sigma_8(z)$.

3 RESULTS

We have carried out the MCMC likelihood analysis of the BOSS DR10 CMASS sample, as well as a large number of the mocks. The parameters that we have included are $H(0.57)$, $D_{\rm A}(0.57)$, β, $\Omega_{\rm m}h^2$, $\Omega_{\rm b}h^2$, $n_{\rm s}$, $P_{\rm norm}$, $\Delta\alpha$, $\sigma_{\rm v}$, $k_\star$, $f_{\rm g}(0.57)$, Q, and $f_{\rm A}$. The dimensionless normalization parameter is given as $P_{\rm norm} = P_0 b^2(0.57)G^2(0.57)[h\ {\rm Mpc}^{-1}]^{n_s+3}$.

In post-processing of the MCMC chains, we also derive constraints on three key parameter combinations that are well constrained and insensitive to systematic effects:

$$x_h(0.57) \equiv H(0.57)r_{\rm s}(z_{\rm d})/c \quad (34)$$

$$x_d(0.57) \equiv D_{\rm A}(0.57)/r_s(z_{\rm d}) \quad (35)$$

$$f_{\rm g}(0.57)\sigma_8(0.57) = I_0^{1/2}P_{\rm norm}^{1/2}\beta, \quad (36)$$

where we have defined

$$I_0 \equiv \int_0^\infty {\rm d}\bar{k}\,\frac{\bar{k}^{n_{\rm s}+2}}{2\pi^2}\,T^2(\bar{k}\cdot h{\rm Mpc}^{-1})\left[\frac{3j_1(8\bar{k})}{8\bar{k}}\right]^2, \quad (37)$$

where $\bar{k} \equiv k/[h\ {\rm Mpc}^{-1}]$ and $j_1(kr)$ is spherical Bessel function. Note that the use of σ_8 does introduce an explicit h-dependence since $\sigma_8 \propto I_0 = I_0(\Omega_{\rm m}h^2, \Omega_{\rm b}h^2, n_{\rm s}, h)$; we compute I_0 with $h = 0.7$ from the fiducial model. An alternative is to use $f_{\rm g}(z)\sigma_m(z)$ as suggested by Wang, Chuang & Hirata (2013), with $\sigma_m(z) \equiv G(z)P_0h^3/({\rm Mpc})^{3+n_{\rm s}}$. We have used $f_{\rm g}(z)\sigma_8(z)$ here for comparison with the published results in the literature. It is reassuring that the measured 2DCF does not depend on h, since $k_\parallel$ and $k_\perp$ scale as $H(z)$ and $1/D_A(z)$, respectively (Wang et al. 2013).

To facilitate easy comparison between data and models, we define the comoving sound horizon at the drag epoch $z_{\rm d}$ as given by

$$\begin{aligned} r_{\rm s}(z_{\rm d}) &= \int_0^t \frac{c_{\rm s}\,{\rm d}t'}{a} = cH_0^{-1}\int_z^\infty {\rm d}z'\,\frac{c_{\rm s}}{E(z')}, \\ &= cH_0^{-1}\int_0^a \frac{{\rm d}a'}{\sqrt{3(1+\overline{R_b}\,a')\,a'^4E^2(z')}} \\ &= \frac{2997.9\,{\rm Mpc}}{\sqrt{0.75\overline{R_b}\omega_m}}\,\ln\left\{\frac{\sqrt{a_d+a_{\rm eq}}+\sqrt{a_d+\overline{R_b}^{-1}}}{\sqrt{a_{\rm eq}}+\sqrt{\overline{R_b}^{-1}}}\right\}, \end{aligned} \quad (38)$$

where a is the cosmic scale factor, $a = 1/(1+z)$; $a^4E^2(z) = \Omega_{\rm m}(a+a_{\rm eq}) + \Omega_k a^2 + \Omega_X X(z)a^4$, with $a_{\rm eq} = \Omega_{\rm rad}/\Omega_{\rm m} = 1/(1+z_{\rm eq})$, and $z_{\rm eq} = 2.5\times10^4\Omega_{\rm m}h^2(T_{\rm CMB}/2.7\,{\rm K})^{-4}$. The sound speed is $c_{\rm s} = 1/\sqrt{3(1+\overline{R_b}\,a)}$, with $\overline{R_b}\,a = 3\rho_b/(4\rho_\gamma)$, $\overline{R_b} = 31\,500\,\Omega_{\rm b}h^2(T_{\rm CMB}/2.7\,{\rm K})^{-4}$. We take $T_{\rm CMB} = 2.72548$ (Fixsen 2009). We assume the redshift of the drag epoch $z_{\rm d}$ to be (Eisenstein & Hu 1998)

$$z_{\rm d} = \frac{1291(\Omega_{\rm m}h^2)^{0.251}}{1+0.659(\Omega_{\rm m}h^2)^{0.828}}\left[1+b_1(\Omega_{\rm b}h^2)^{b2}\right], \quad (39)$$

with

$$b_1 = 0.313(\Omega_{\rm m}h^2)^{-0.419}\left[1+0.607(\Omega_{\rm m}h^2)^{0.674}\right],$$
$$b_2 = 0.238(\Omega_{\rm m}h^2)^{0.223}. \quad (40)$$

Our choice for $r_s(z_d)$ differs from that of the BOSS team, who have chosen to define $r_s(z_d)$ as the value computed numerically by CAMB. For a given cosmological model, our $r_s(z_d)$ value from equations (38)–(40) differs from that given by CAMB by a factor that is close to one and nearly independent of the cosmological model (Mehta et al. 2012). Since $r_s(z_d)$ is only used to scale $H(z)$ and $D_A(z)$, the comparison between data and models should be insensitive to the choice of $r_s(z_d)$, as long as we are consistent in using the same definition of $r_s(z_d)$ in analysing data and making model predictions.

We apply flat priors on all the parameters. The priors on the parameters that are well constrained by the data, $H(0.57)$, $D_A(0.57)$, β, $\Omega_m h^2$, P_{norm}, $\Delta\alpha$, are sufficiently wide so that the results are insensitive to the ranges chosen. We impose flat priors of $\Omega_b h^2 = (0.02018, 0.02438)$, $n_s = (0.9137, 1.0187)$, corresponding to the 7σ range of these parameters from the first-year *Planck* data, with σ from the Gaussian fits by Wang & Wang (2013); these wide priors ensure that cosmic microwave background (CMB) constraints are not double counted when our results are combined with CMB data (Chuang, Wang & Hemantha 2012). Our results are not sensitive to the parameters that describe the systematic uncertainties: $k_\star$, $f_g(0.57)$, σ_v, Q, A; we impose reasonable flat priors on these: $k_\star = (0.1, 0.3)$, $f_g(0.57) = 0.35 - 0.55$, $\sigma_v < 500\,\mathrm{km\,s^{-1}}$, $Q = 0 - 40\,(\mathrm{Mpc}/h)^2$, and $f_A = 0$–$10\ \mathrm{Mpc}\,h^{-1}$.

3.1 Validation using mocks

Fig. 1 shows the BOSS DR10 CMASS sample (upper panel) and a representative mock (lower panel). The contour levels are $\xi = 0.0025, 0.005, 0.01, 0.025, 0.1, 0.5, 2.0$; the dotted contours denote $\xi \leq 0$. The solid lines are the data (or mock data), and the dashed lines are our best-fitting model. The comparison of Fig. 1 (BOSS DR10) with fig. 1 in Wang (2014) (BOSS DR9) shows the significant expansion in the range over which the 2DCF from data is well determined. The bottom panel in Fig. 1 clearly shows that our model applies even on small scales. The shaded disc indicates the range of scales that we will use in our MCMC likelihood analysis to measure $H(z)$, $D_A(z)$, and $f_g(z)$, 16–144 h^{-1} Mpc.

We have analysed 264 mocks of the BOSS DR10 CMASS sample using MCMC likelihood analysis, in the scale range of 16–144 h^{-1} Mpc. To speed up computation, we fixed the non-linearity parameters Q and f_A to fiducial values of $Q = 13$ and $f_A = 1.5$. We find that including the data at $\sigma < 8\,h^{-1}$ Mpc leads to high noise levels, and results in $f_g(0.57)\sigma_8(0.57)$ measurements that are biased high compared to the true value. However, discarding the data at $\sigma < 8\,h^{-1}$ Mpc leads to $H(0.57)$ measurements that are biased low compared to the true value. The data contours (upper panel in Fig. 1) suggest that we discard the data at $\sigma < 8\,h^{-1}$ Mpc for $\pi > 48\,h^{-1}$ Mpc only, so that we can use the less noisy data near the line of sight on intermediate scales. We find that this cut leads to unbiased estimates of $x_h = H(0.57)\,r_s(z_d)/c$, $x_d = D_A(0.57)/r_s(z_d)$, and $f_g(0.57)\sigma_8(0.57)$.

Fig. 2 presents the resultant likelihood peak distributions of $x_h(0.57)$, $x_d(0.57)$, and $f_g(0.57)\sigma_8(0.57)$ from 264 mocks with the scale range of 16–144 h^{-1} Mpc (solid lines), and 252 mocks with the scale range of 32–144 h^{-1} Mpc (dashed lines). These show the distributions of the best-fitting values from the mocks. The dotted lines indicate the values predicted by the input model of the mocks. The true values of x_h, x_d, and $f_g\sigma_8$ are all near the mean values in the distributions of the best-fitting values for the scale range of 16–144 h^{-1} Mpc, but are somewhat farther away from the mean values for the scale range of 32–144 h^{-1} Mpc. This indicates that our modelling works remarkably well for the scale range of

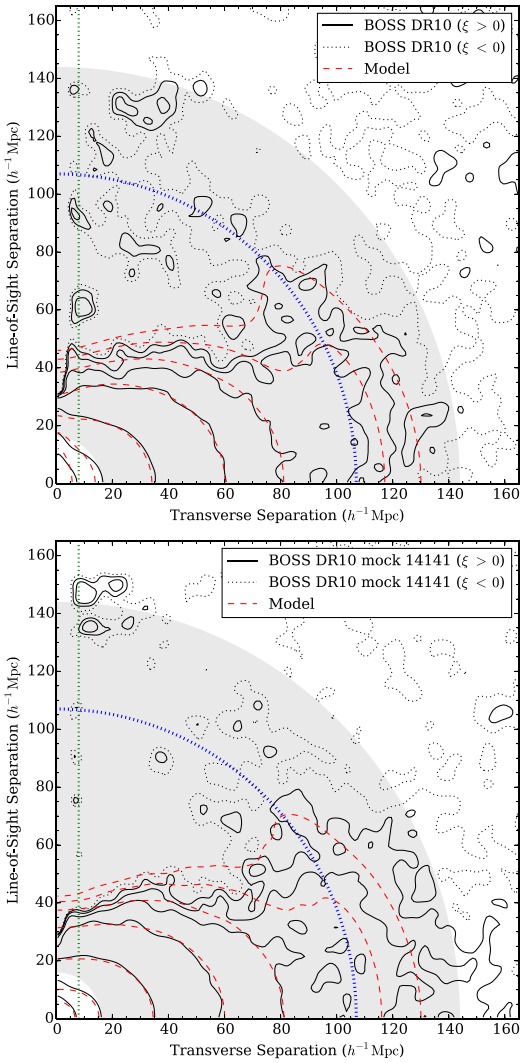

Figure 1. The BOSS DR10 CMASS sample (upper panel) and a representative mock (lower panel). The contour levels are $\xi = 0.0025, 0.005, 0.01, 0.025, 0.1, 0.5, 2.0$, with the dotted contours denoting $\xi \leq 0$. The solid lines are the data (or mock data); the dashed lines are our best-fitting model.

16–144 h^{-1} Mpc, giving unbiased parameter estimates. For the scale range of 32–144 h^{-1} Mpc, the parameter estimates are slightly biased. Comparing our Fig. 2 with fig. 2 of Wang (2014), one can see that our current modelling significantly improves the recovery of the true $H(0.57)$.

Note that we have plotted the best-fitting values, and not the marginalized means, of $x_h(0.57)$, $x_d(0.57)$, and $f_g(0.57)\sigma_8(0.57)$ from the mocks. This is because the best-fitting values are obtained much more quickly than the converged marginalized means (which are sensitive to the tails of the distributions). As the MCMC chains converge, the marginalized means approach the likelihood peak (i.e. the best-fitting) values, and the two become very similar (Lewis & Bridle 2002).

3.2 Results from BOSS DR10 CMASS sample

We now present our results from analysing the real data, the BOSS DR10 CMASS sample. We use the same methodology as we have used for the mocks. Table 1 lists the χ^2 per degree of freedom from the different cases that we have studied. The 'σ and π cut' refers to

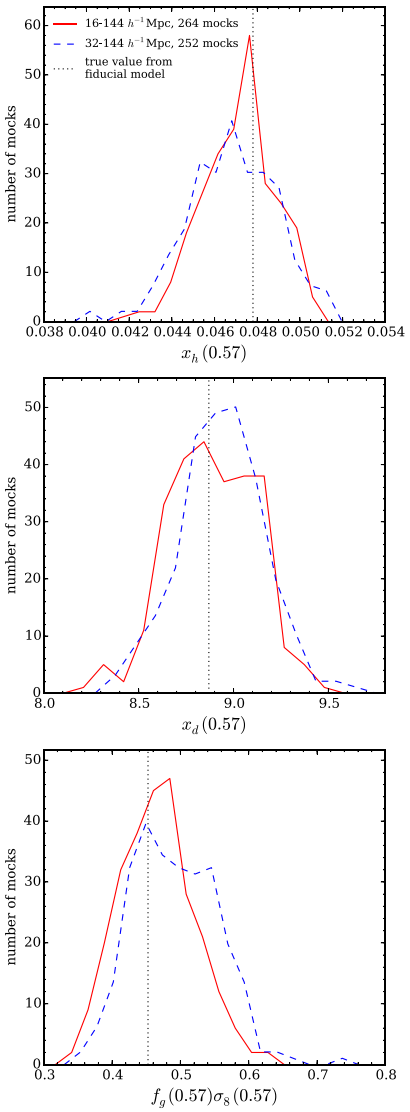

Figure 2. The distribution of best-fitting values of $x_h(0.57) = H(0.57)\,r_s(z_d)/c$, $x_d(0.57) = D_A(0.57)/r_s(z_d)$, and $f_g(0.57)\sigma_8(0.57)$ from 264 mocks of the BOSS DR10 CMASS sample with the scale range of 16–144 h^{-1} Mpc (solid lines), and 252 mocks with the scale range of 32–144 h^{-1} Mpc (dashed lines). The dotted lines indicate the values predicted by the input model of the mocks.

excluding the narrow wedge along the line of sight at $\sigma < 8\,h^{-1}$ Mpc for $\pi > 48\,h^{-1}$ Mpc, the same cut as we used for the mocks. All four cases with the σ and π cut have $\chi^2_{\rm pdf} \simeq 1$, whereas the no σ and π cut case has $\chi^2_{\rm pdf} \simeq 1.5$; this supports our choice of making the σ and π cut in the remainder of our analysis.

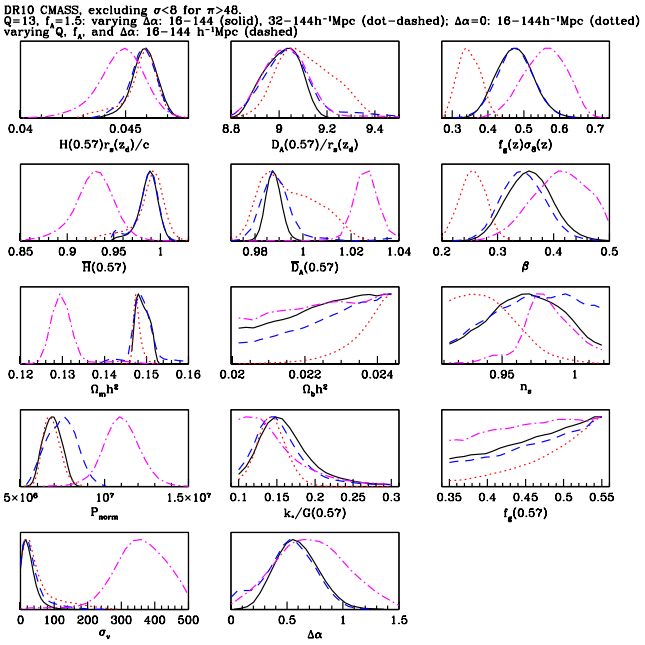

Figure 3. The 1D marginalized probability distribution of parameters estimated from the BOSS DR10 CMASS sample, excluding $\sigma < 8\,h^{-1}$ Mpc for $\pi > 48\,h^{-1}$ Mpc. The different line types represent different choices made in our analysis (all are tabulated in Table 1). The solid lines are for the scale range of 16–144h^{-1} Mpc, varying $\Delta\alpha$, $Q = 13$, $f_A = 1.5$. The dot–dashed lines are for the scale range of 32–144h^{-1} Mpc, varying $\Delta\alpha$, $Q = 13$, $f_A = 1.5$. The dotted lines are for the scale range of 16–144h^{-1} Mpc, $\Delta\alpha = 0$, $Q = 13$, $f_A = 1.5$. The dashed lines are for the scale range of 16–144h^{-1} Mpc, varying $\Delta\alpha$, Q, and f_A.

Fig. 3 shows the 1D marginalized probability distribution of parameters measured from BOSS DR10 CMASS sample, for the four cases in Table 1 with the σ and π cut. The solid lines are results for the scale range 16–144 h^{-1} Mpc, with non-linearity parameters $Q = 13$ and $f_A = 1.5$. The dashed lines show what happens if we vary Q and f_A: the constraints on $H(0.57)\,r_s(z_d)/c$, $D_A(0.57)/r_s(z_d)$, and $f_g(0.57)\sigma_8(0.57)$ remain essentially unchanged. The slight differences are due to the MCMC chains with varying Q and f_A not having fully converged; these are very slow to converge due to the weak constraints on Q and f_A from data.

The dot–dashed lines in Fig. 3 show the results of choosing a narrower scale range that leaves out the smallest scale information: 32–144 h^{-1} Mpc. We find that not using the small-scale information from 16–32 h^{-1} Mpc leads to a much weaker constraint on $H(0.57)\,r_s(z_d)/c$, and higher values for $f_g(0.57)\sigma_8(0.57)$, while having only a minor impact on the constraints on $D_A(0.57)/r_s(z_d)$. It is surprising that the scale ranges 16–144 h^{-1} Mpc and 32–144 h^{-1} Mpc give significantly different constraints on $H(0.57)$, $D_A(0.57)$, and $\Omega_m h^2$; this suggests that there are significant

Table 1. χ^2 per degree of freedom in the modelling of the BOSS DR10 CMASS sample, for different data selection and modelling choices.

Scale range	σ and π cut	$\Delta\alpha$	(Q, f_A)	$N_{\rm data}$	$N_{\rm par}$	$\chi^2_{\rm min}$	$\chi^2_{\rm pdf}$	Comment
16–144 h^{-1} Mpc	Yes	Varied	(13, 1.5)	240	11	248.5	1.09	Validated by mocks
32–144 h^{-1} Mpc	Yes	Varied	(13, 1.5)	230	11	209.0	0.95	High $f_g(0.57)\sigma_8(0.57)$
16–144 h^{-1} Mpc	No	Varied	(13, 1.5)	252	11	355.0	1.47	High $f_g(0.57)\sigma_8(0.57)$
16–144 h^{-1} Mpc	Yes	Zero	(13, 1.5)	240	10	255.7	1.11	Low $f_g(0.57)\sigma_8(0.57)$
16–144 h^{-1} Mpc	Yes	Varied	Varied	240	13	244.7	1.08	Slow convergence

Table 2. The mean and standard deviation of $\{H(0.57)$, $D_A(0.57)$, $\Omega_m h^2$, β, $H(0.57)\, r_s(z_d)/c$, $D_A(0.57)/r_s(z_d)$, $f(0.57)\,\sigma_8(0.57)\}$ from BOSS DR10 CMASS sample, for the scale ranges $16 < s < 144h^{-1}$ Mpc and $32 < s < 144h^{-1}$ Mpc (excluding $\sigma < 8\,h^{-1}$ Mpc for $\pi > 48\,h^{-1}$ Mpc). The unit of H is km s^{-1} Mpc^{-1}. The unit of D_A is Mpc.

	$16 < s < 144$	$32 < s < 144$
$H(0.57)$	92.36 ± 0.98	86.95 ± 1.96
$D_A(0.57)$	1343.00 ± 4.26	1395.51 ± 7.85
$\Omega_m h^2$	0.1492 ± 0.0014	0.1304 ± 0.0037
β	0.358 ± 0.039	0.412 ± 0.048
$H(0.57)\, r_s(z_d)/c$	0.0459 ± 0.0006	0.0448 ± 0.0011
$D_A(0.57)/r_s(z_d)$	9.0107 ± 0.0729	9.0353 ± 0.1050
$f(0.57)\,\sigma_8(0.57)$	0.4757 ± 0.0497	0.5583 ± 0.0579

degeneracies in fitting the model to the data, with the addition of the small-scale data breaking the degeneracy. It is reassuring that the two scale ranges give similar constraints on the physical parameters $H(0.57)\, r_s(z_d)/c$ and $D_A(0.57)/r_s(z_d)$, in agreement with the results from the mocks (see Fig. 2).

The dotted lines in Fig. 3 show the results from setting $\Delta\alpha = 0$, i.e. not using the RSD modelling from Zheng et al. (2013), for the scale range of 16–144 h^{-1} Mpc. This has a minimal impact on the $H(0.57)\, r_s(z_d)/c$ measurement, but significantly weakens the $D_A(0.57)/r_s(z_d)$ measurement, and leads to very low values for $f_g(0.57)\sigma_8(0.57)$. This is not surprising; the measurement of the growth rate is highly sensitive to the modelling of RSD on small scales.

Table 2 gives the marginalized means and standard deviations of $\{H(0.57), D_A(0.57), \Omega_m h^2, \beta, H(0.57)\, r_s(z_d)/c, D_A(0.57)/r_s(z_d), f(0.57)\,\sigma_8(0.57)\}$ from BOSS DR10 CMASS sample, for the scale ranges $16 < s < 144h^{-1}$ Mpc and $32 < s < 144h^{-1}$ Mpc (excluding $\sigma < 8\,h^{-1}$ Mpc for $\pi > 48\,h^{-1}$ Mpc). The differences between the constraints on $\{H(0.57)\, r_s(z_d)/c, D_A(0.57)/r_s(z_d), f(0.57)\,\sigma_8(0.57)\}$ for the two different scale ranges are in qualitative agreement with that found using mocks (see Fig. 2). Since the mocks show that the $f(0.57)\,\sigma_8(0.57)$ measurements from $16 < s < 144h^{-1}$ Mpc are unbiased, we draw the same conclusion about the measurements from the real data. This implies that the $f(0.57)\,\sigma_8(0.57)$ measurement from $32 < s < 144h^{-1}$ Mpc from the real data is biased high. Note that while the measurements of $f(0.57)\,\sigma_8(0.57)$ differ significantly for the two scale ranges, they overlap at 1σ, indicating that the difference is statistically consistent with the predictions from the mocks. Table 3 shows the corresponding normalized covariance matrix for the case with the validated scale range of $16 < s < 144h^{-1}$ Mpc.

4 SUMMARY AND DISCUSSION

Galaxy clustering is a key probe of dark energy and modified gravity. Much of its ultimate power will come from small scales, which can only be included in the data analysis if we can reliably model galaxy clustering on these scales. We have presented a new approach to measuring cosmic expansion history and growth rate of large-scale structure using the anisotropic 2DCF measured from data over the wide scale range of 16–144 h^{-1} Mpc, reaching down to a significantly smaller scale than in previous work. Our modelling of galaxy clustering uses the empirical modelling of small-scale galaxy clustering derived from numerical simulations by Zheng et al. (2013, see equations 1–3) which provides improved fit to RSD and non-linear effects on small scales. We have validated our methodology using mock catalogues, finding it to enable accurate and precise measurements of cosmic expansion history and growth rate of large-scale structure.

Applying our methodology to the analysis of the 2DCF of galaxies from the BOSS DR10 CMASS sample, in the scale range of 16–144 h^{-1} Mpc (excluding the noisy data in the small line-of-sight wedge beyond 48 h^{-1} Mpc), we measure $H(0.57)r_s(z_d)/c$, $D_A(0.57)/r_s(z_d)$, and $f_g(0.57)\sigma_8(0.57)$ with precisions of 1.3 per cent, 0.8 per cent, and 10.5 per cent, respectively (see Table 2). These are significantly tighter than those obtained by others using the same data, see e.g. Anderson et al. (2014). This is not surprising since we have utilized significantly more information from data.

It is often assumed that discarding small-scale information leads to more robust measurements of $H(z)$ and $D_A(z)$. We find that neglecting the small-scale information weakens the constraints on $H(z)r_s(z_d)$ and $D_A(z)/r_s(z_d)$, as expected (see Fig. 3). Interestingly, omitting the small-scale information seems to favour a low matter density, along with a low $H(z)$ and a high $D_A(z)$, which combine to give roughly the same $H(z)r_s(z_d)$ and $D_A(z)/r_s(z_d)$ but with larger uncertainties, compared to including the small-scale information. This indicates that the measurements of $H(z)r_s(z_d)$ and $D_A(z)/r_s(z_d)$ are more robust than that of $H(z)$ and $D_A(z)$.

We find that the measurement of $f_g(z)\sigma_8(z)$ is very sensitive to the RSD modelling. Not including the improved RSD modelling from Zheng et al. (2013) leads to an estimate of $f_g(z)\sigma_8(z)$ that is biased low significantly (see Fig. 3). On the other hand, omitting the small-scale information, even when using the RSD modelling from Zheng et al. (2013), leads to an estimate of $f_g(z)\sigma_8(z)$ that is biased somewhat high. Our conclusion that the $f_g(z)\sigma_8(z)$ measurement from $32 < s < 144h^{-1}$ Mpc is biased high (while that from $16 < s < 144h^{-1}$ Mpc is unbiased) is based on tests using the mocks (see Fig. 2). The trends discussed above may explain in part the wide range of $f_g(0.57)\sigma_8(0.57)$ measurements from BOSS data that have been reported in the literature.

Table 3. Normalized covariance matrix of the measured and derived parameters, $\{H(0.57)$, $D_A(0.57)$, $\Omega_m h^2$, β,, $H(0.57)\, r_{as}(z_d)/c$, $D_A(0.57)/r_s(z_d)$, $f(0.57)\sigma_8(0.57)\}$, from the BOSS DR10 CMASS sample for the scale range of $16 < s < 144h^{-1}$ Mpc.

	$H(0.57)$	$D_A(0.57)$	$\Omega_m h^2$	β	$H(0.57)\, r_s(z_d)/c$	$D_A(0.57)/r_s(z_d)$	$f(0.57)\sigma_8(0.57)$
$H(0.57)$	1.0000	0.3191	−0.0092	0.1748	0.8239	0.0879	0.1104
$D_A(0.57)$	0.3191	1.0000	−0.0983	0.0899	0.2592	0.3856	0.1016
$\Omega_m h^2$	−0.0092	−0.0983	1.0000	0.0243	−0.2370	0.3364	0.0411
β	0.1748	0.0899	0.0243	1.0000	0.1558	0.0098	0.9845
$H(0.57)\, r_s(z_d)/c$	0.8239	0.2592	−0.2370	0.1558	1.0000	−0.4514	0.1115
$D_A(0.57)/r_s(z_d)$	0.0879	0.3856	0.3364	0.0098	−0.4514	1.0000	0.0025
$f(0.57)\sigma_8(0.57)$	0.1104	0.1016	0.0411	0.9845	0.1115	0.0025	1.0000

It is surprising that using the data in the scale ranges of $16 < s < 144h^{-1}$ Mpc and $32 < s < 144h^{-1}$ Mpc gives very different constraints on $H(0.57)$, $D_A(0.57)$, and $\Omega_m h^2$ (see Table 2). These two scale ranges do give similar constraints for the physical parameters $H(0.57)r_s(z_d)/c$, $D_A(0.57)/r_s(z_d)$, with the differences in qualitative agreement with the results from mocks (see Fig. 2). This suggests that the different constraints on $H(0.57)$, $D_A(0.57)$, and $\Omega_m h^2$ result from degeneracies in fitting the model to the data; the addition of the small-scale data breaks this degeneracy. This indicates that $H(0.57)r_s(z_d)/c$ and $D_A(0.57)/r_s(z_d)$, instead of $H(0.57)$, $D_A(0.57)$, and $\Omega_m h^2$, should be used to summarize BAO constraints.

Another surprise may be how well our model fits, since we used the model from Zheng et al. (2013, based on Zhang et al. 2013), which is similar to the model proposed by Scoccimarro (2004), which is not expected to be accurate beyond $k = 0.1\,h$ Mpc^{-1}, or a scale of 40–$50\,h^{-1}$ Mpc. The difference between Scoccimarro (2004) and Zhang et al. (2013) is that the earlier work did not explicitly make the RSD model corrections a modification to the linear model by Kaiser (1987) in the form of a window function. The introduction of the window function by Zhang et al. (2013) allows a compact formulation for the RSD model that is easily implemented in the framework from Wang (2014), which already includes a correction factor for non-linear evolution and scale-dependent bias (see equation 5), as well as the dewiggled power spectrum (see equations 6–8), with asymmetric damping that accounts for the damping of the BAO peak due to non-linear effects. Our new model, presented in this paper, combines these three models, with the parameters in each determined by data. This proves adequate for fitting the BOSS DR10 data.

We have not included massive neutrinos in our analysis, since they would likely have a small effect, and are computationally expensive. However, it is important to include massive neutrinos in data analysis; we will do so in future work.

Our results are encouraging, and indicate that we can significantly tighten constraints on dark energy and modified gravity by reliably modelling small-scale galaxy clustering. We will apply our methodology to BOSS DR12 data, once they are publicly available. We will also include this new approach in the forecasting of constraints on dark energy and gravity for *Euclid* and *WFIRST*.

ACKNOWLEDGEMENTS

The analysis of the mocks was carried out on the supercomputing clusters at Jet Propulsion Laboratory. I am grateful to Chia-Hsun Chuang for sharing the 2DCF of the BOSS DR10 CMASS sample and the 600 mocks, and Alex Merson for helping me make Figs. 1 and 2 using PYTHON.

Funding for SDSS-III has been provided by the Alfred P. Sloan Foundation, the Participating Institutions, the National Science Foundation, and the US Department of Energy Office of Science. The SDSS-III website is http://www.sdss3.org/.

SDSS-III is managed by the Astrophysical Research Consortium for the Participating Institutions of the SDSS-III Collaboration including the University of Arizona, the Brazilian Participation Group, Brookhaven National Laboratory, Carnegie Mellon University, University of Florida, the French Participation Group, the German Participation Group, Harvard University, the Instituto de Astrofisica de Canarias, the Michigan State/Notre Dame/JINA Participation Group, Johns Hopkins University, Lawrence Berkeley National Laboratory, Max Planck Institute for Astrophysics, Max Planck Institute for Extraterrestrial Physics, New Mexico State University, New York University, Ohio State University, Pennsylvania State University, University of Portsmouth, Princeton University, the Spanish Participation Group, University of Tokyo, University of Utah, Vanderbilt University, University of Virginia, University of Washington, and Yale University.

REFERENCES

Anderson L. et al., 2014, MNRAS, 441, 24
Blake C., Glazebrook G., 2003, ApJ, 594, 665
Caldwell R. R., Kamionkowski M., 2009, Ann. Rev. Nucl. Part. Sci., 59, 397
Chuang C.-H., Wang Y., 2012, MNRAS, 426, 226
Chuang C.-H., Wang Y., 2013, MNRAS, 435, 255
Chuang C.-H., Wang Y., Hemantha M., 2012, MNRAS, 423, 1474
Cole S. et al., 2005, MNRAS, 362, 505
Eisenstein D. J., Hu W.1998, ApJ, 496, 605
Eisenstein D. J., Seo H.-J., White M., 2007, ApJ, 664, 660
Fixsen D. J., 2009, ApJ, 707, 916
Frieman J., Turner M., Huterer D., 2008, ARA&A, 46, 385
Guzzo L. et al., 2008, Nature, 451, 541
Hamilton A. J. S., 1992, ApJ, 385, L5
Hartlap J., Simon P., Schneider P., 2007, A&A, 464, 399
Kaiser N., 1987, MNRAS, 227, 1
Landy S. D., Szalay A. S., 1993, ApJ, 412, 64
Laureijs R. et al., 2011, Euclid Definition Study Report, preprint (arXiv:1110.3193)
Lewis A., Bridle S., 2002, Phys. Rev. D, 66, 103511
Li M., Li X.-D., Wang S., Wang Y., 2011, Commun. Theor. Phys., 56, 525
Manera M. et al., 2013, MNRAS, 428, 1036
Manera M. et al., 2015, MNRAS, 447, 437
Mehta K., Cuesta A. J., Xu X., Eisenstein D. J., Padmanabhan N., 2012, MNRAS, 427, 2168
Perlmutter S. et al., 1999, ApJ, 517, 565
Press W. H., Teukolsky S. A., Vetterling W. T., Flannery B. P., 1992, Numerical Recipes in C. The Art of Scientific Computing, 2nd edn. Cambridge Univ. Press, Cambridge
Ratra B., Vogeley M. S., 2008, PASP, 120, 235
Riess A. et al., 1998, AJ, 116, 1009
Samushia L. et al., 2013, MNRAS, 439, 3504
Sanchez A. G., 2013, MNRAS, 440, 2692
Sanchez A. G., Baugh C. M., Angulo R., 2008, MNRAS, 390, 1470
Scoccimarro R., 2004, Phys. Rev. D, 70, 083007
Seo H., Eisenstein D., 2003, ApJ, 598, 720
Song Y.-S., Percival W. J., 2009, J. Cosmol. Astropart. Phys., 0910, 004
Spergel D. et al., 2015, Wide-Field InfrarRed Survey Telescope-Astrophysics Focused Telescope Assets WFIRST-AFTA 2015 Report, preprint (arXiv:1503.03757)
Uzan J.-P., 2010, Gen. Relativ. Gravit., 42, 2219
Wang Y., 2008, J. Cosmol. Astropart. Phys., 0805, 021
Wang Y., 2010, Dark Energy. Wiley-VCH, New York
Wang Y., 2014, MNRAS, 443, 2950
Wang Y., Wang S., 2013, Phys. Rev. D, 88, 043522
Wang Y., Chuang C.-H., Hirata C. M., 2013, MNRAS, 430, 2446
Weinberg D. H., Mortonson M. J., Eisenstein D. J., Hirata C., Riess A. G., Rozo E., 2013, Phys. Rep., 530, 87
Zhang P.-J., Pan J., Zheng Y., 2013, Phys. Rev. D, 87, 063526
Zheng Y., Zhang P.-J., Jing Y.-P., Lin W.-P., Pan J., 2013, Phys. Rev. D, 88, 103510

This paper has been typeset from a TEX/LATEX file prepared by the author.